Journal of The Electrochemical Society, 2022 **169** 026519
1945-7111/2022/169(2)/026519/6/$40.00 © 2022 The Electrochemical Society ("ECS"). Published on behalf of ECS by IOP Publishing Limited

The Substrate Morphology Effect for Sulfur-Rich Amorphous Molybdenum Sulfide for Electrochemical Hydrogen Evolution Reaction

Marina Medina, Patricia G. Corradini,[a] Juliana F. de Brito, Hugo L. Sousa Santos, and Lucia Helena Mascaro[z]

Department of Chemistry, Federal University of São Carlos, CEP 13565-905, São Carlos-SP, Brazil

Amorphous molybdenum sulfide (MoS_x) is a promising material for hydrogen evolution reaction (HER) due to its nearly zero hydrogen adsorption free energy at the sulfur (S) edge-sites. To prepare more efficient MoS_x-based electrocatalysts, new attempts are required to increase the exposure of the MoS_x lateral size and, therefore, increase the S atom's contents. The majority of studies reported in the literature investigate MoS_x over conductive substrates. However, MoS_x can be electrodeposited over inexpensive and chemically stable platforms, such as semiconductors. This work presents the semiconductor substrate morphology effect for prepared sulfur-rich MoS_x for electrochemical hydrogen evolution reaction. The electrodes are prepared by cyclic voltammetry with 25 cycles over TiO_2 film and TiO_2 nanotubes (TiO_2NT) substrates. The MoS_x deposit on TiO_2NT presents an increase S atoms contents and exhibits excellent HER activity with a low overpotential of 93 ± 7.5 mV to reach -10 mA cm^{-2} and a higher exchange current density equal to 91 μA cm^{-2}, and a smaller Tafel slope of 43 mV dec^{-1}.
 [DOI: 10.1149/1945-7111/ac5067]

Manuscript submitted November 2, 2021; revised manuscript received January 10, 2022. Published February 16, 2022. *This paper is part of the JES Focus Issue on Women in Electrochemistry.*

Supplementary material for this article is available online

The development of low-cost catalyst materials that are highly efficient for electrochemical water splitting is crucial for the implementation of hydrogen as an alternative energy carrier, replacing the majority use of carbon-based fuels.[1–4] Among the possible ways to produce hydrogen, the electrochemical water splitting is the faster one and the product obtained is the cleanest.[3] The process is divided into the hydrogen evolution reaction (HER) that occurs in the cathode, and the oxygen evolution reaction (OER) at the anode.[1] To increase the hydrogen production yield, a highly efficient catalyst material is necessary. Platinum (Pt) is the most efficient but factors as high cost due to scarcity limit its large-scale application.[5]

In electrocatalysis, Gibb´s free energy for hydrogen adsorption in the active site is an important reactivity parameter when looking for alternative materials.[6] In this sense, electrocatalysts based on molybdenum sulfides (MoS_2) are some of the most promising candidates for HER catalysis application, due to its low Gibb´s free energy value (0.08 eV) for hydrogen adsorption at the S edge sites.[7] Like other transition metal sulfides, the basal plane of the crystalline MoS_2 is inactive for hydrogen production while the edge-sites formed by Mo and S coordinatively unsaturated is the active one. Based on that, the amorphous molybdenum sulfide (MoS_x), plenty of these unsaturated regions, presents higher catalytic activity than the crystalline form.[8,9]

Analyzing if Mo or S atoms is the active site for the proton reduction, Deng and co-workers pinpointed that the S atoms are the active one.[10] Beyond that, among the three types of S configurations (terminal S_2^{2-}, apical S^{2-}, bridging S_2^{2-}), experimental and theoretical investigations show that the bridging ligand is the major active site for proton reduction.[11–14] Yeo co-workers show that H adsorbs weakly on apical S^{2-} atoms while the greater content of bridging S_2^{2-} over the terminal S_2^{2} is responsible for the increased turnover frequency (TOF) of hydrogen evolution.[13] Lee and co-workers reported the aging approach to maximize the bridging S_2^{2-} in MoS_x by the addition of ammonium polysulfide, reaching -10 mA cm^{-2} at -96 mV and a Tafel slope of 46 mV dec^{-1}.[11]

The substrate used to support the catalyst acts as an injector or collector of the charge carriers formed in the electrocatalysis process. Beyond that, the type of interactions in the junction between the support and the catalyst is decisive for the electrocatalyst's performance. Nørskov and co-workers verified that strong adhesion of the MoS_2 catalyst onto the substrate leads to the weakening in the hydrogen bonding and the consequent decrease in the H_2 production.[15] More recently, Xie and co-workers found that the carbon nanotubes benefits the exposure of S active sites as a consequence of the suppression of oriented in-plane growth of MoS_2 due to weak van der Walls interactions between the support and the catalyst.[16]

Based on the mentioned above, we hypothesize that the growth of an amorphous MoS_x film on TiO_2 nanotubes (TiO_2NT) semiconductor substrate can increase the exposure and contents of sulfur atoms due to the possibility of non-oriented MoS_x deposit and boost the catalyst´s performance as a consequence. The semiconductor titanium dioxide nanotube (TiO_2NT) was already used to support MoS_2 materials in different synthesis methods for water splitting.[17–20] However, to the best of our knowledge, this is the first report describing the nanotube substrate effect in the electrodeposition growth pattern of the MoS_x. Thus, the present work reports the preparation by electrodeposition of MoS_x deposit on TiO_2NT and on a TiO_2 film to compare the differences in the catalyst's growth pattern over different substrates morphologies.

Experimental

Preparation of titanium dioxide nanotubes (TiO_2 NT) substrate.—The TiO_2 NT semiconductor substrate was prepared by anodization of Ti foil (Sigma Aldrich®, 99.7%) according to Bessegato and co-workers' methodology.[21,22] First, the Ti foil was cleaned in three steps under sonication in acetone, isopropanol, and water for 15 min each, at the end being dried in nitrogen gas (N_2). Second, the titanium foil was used as an anode in an electrochemical cell while the cathode was a ruthenium plate. The anodization was performed using the electrolyte 1.0 mol l^{-1} NaH_2PO_4 with 0.3% HF applying a potential equal to 20 V for 2 h using a DC power supply. After anodization, the electrode was washed with ultrapure water, dried in N_2, and calcined at 450 °C in a muffle furnace for 2 h.

Preparation of TiO_2 film substrate.—Ti plates (2 cm^2; Sigma Aldrich®, 99.7%) were sanded with 400, 600, and 1200 grit sandpaper. Basic degreasing was performed with 10% (w/w) NaOH aqueous solution followed by acid etching in 30% (w/w)

[a]Present address: Fluminense Federal Institute of Education, Science and Technology, Campus Itaperuna, Itaperuna, RJ 28300–000, Brazil.
[z]E-mail: lmascaro@ufscar.br

HCl aqueous solution at 100 °C for 1 h. In the end, the plates were washed in deionized water. TiO_2 thin film was prepared by spin coating method according to Schmuki and co-workers adapted methodology on the pre-treated metallic Ti plate.[23] A volume equal to 100 μl of 30% titanium isopropoxide solution in isopropanol was applied on the Ti plate while it was rotating at 300 rpm for 30 s under N_2 atmosphere. In the end, heat treatment was performed at 450 °C for 2 h in a muffle furnace.

Preparation of MoS_x composites by electrodeposition.—The molybdenum sulfide film was prepared by electrodeposition technique according to our recent report.[24] The cyclic voltammetry (CV) technique was performed by 25 cycles in the potential range of −1.0 to 0.1 V at 50 mV s^{-1} using 4 mmol l^{-1} $(NH_4)_2MoS_4$ (Sigma Aldrich®, 99.97%) and 0.1 mol l^{-1} $NaClO_4$ (Merck®) as the precursor solution. The TiO_2 NT or TiO_2/Ti semiconductor substrates (2 cm^2) was used as the working electrode while a Pt plate (4 cm^2) and $Ag/AgCl/Cl^-_{(sat.\ KCl)}$ were the auxiliary and reference electrodes, respectively. To ensure the deposit of the same amount of the catalyst material on both substrates, the deposition charge was also controlled, reaching a value equal to approximately 14 mC cm^{-2}.

Characterizations.—The micrographs of MoS_x films on TiO_2-based substrates were obtained by scanning electron microscope (SEM), model FEI-Inspect F50. For X-ray Diffraction (XRD) measurements, a Shimadzu XRD—6000 X-ray diffractometer was used. The radiation produced by the copper tube was CuKα with a wavelength of 1.54 Å, which was produced by a 40.0 kV acceleration voltage and 30.0 mA beam current. The 2θ range investigated was from 10° to 60° with a scanning speed of 2.0° min^{-1}. X-ray photoelectron spectra were obtained on a Scienta Omicron (ESCA 2SR) spectrometer with an Al Kα radiation source (1486.7), where the peak positions were calibrated for the 1 s carbon peak at 284.8 eV. CasaXPS software (version 2.3) was used for elemental quantitation from the spectrum and high-resolution deconvolution of the Mo and S elements.

Electrochemical measurements.—The catalytic activity measurements of the MoS_x/TiO_2NT and MoS_x/TiO_2 electrodes were performed in a common three-electrode cell using an Autolab potentiostat/galvanostat electrochemical station. A Pt disc with a diameter equal to 3 mm was used as a working electrode for comparison purposes. The auxiliary and reference electrodes were a Pt plate (4 cm^2) and $Ag/AgCl/Cl^-_{(sat.\ KCl)}$ respectively. An acidic solution of H_2SO_4, pH 0.3, was used as the electrolyte. Linear sweep voltammetry (LSV) was performed at a scan rate of 5 mV s^{-1} and the linear portion was fitted for Tafel plot based on the Tafel equation:

$$\eta = a + b \log j \qquad [1]$$

where η is the overpotential (V), j is the current density (A cm^{-2}) and b is the Tafel slope (V dec^{-1}).

The electrochemical active surface area was evaluated by CV at different scan rates: 10, 20, 40, and 80 mV s^{-1}. Electrochemical impedance spectroscopy (EIS) was performed at −0.347 V vs $Ag/AgCl/Cl^-_{(sat.\ KCl)}$ with an applied frequency ranging from 10 kHz to 0.1 Hz and a potential amplitude of 5 mV. The measured potential, $E_{Ag/AgCl/Cl-(sat.\ KCl)}$, was converted to the potential of a regular hydrogen electrode, E_{RHE}, according to the Nernst equation:[25]

$$E_{RHE} = E_{Ag/AgCl/Cl^-(sat.\ KCl)} + 0.197 + (0.059\ pH) \qquad [2]$$

Calculation of turnover frequency (TOF)

To perform the TOF calculation a faradaic efficiency of 100% was considered and the following equation was used:

$$TOF = \frac{Number\ of\ total\ hydrogen/cm^2}{Number\ of\ active\ sites/cm^2} \qquad [3]$$

The current density at −200 mV was used to calculate the total number of hydrogen atoms evolved, while the number of active sites on the electrode was calculated following the analyses shows by Benck and co-workers,[26] described in the Supporting Information (SI) (Table SV).

Results and Discussion

The MoS_x electrodeposition was conducted on TiO_2NT and TiO_2 film substrates in the same way over 25 cycles in the cyclic voltammetry method to guarantee that the same catalyst amount was deposit on both substrates. The cyclic voltammograms are presented in Figs. 1a, 1b, for TiO_2NT and TiO_2 film, respectively.

The voltammetric curves present a rise in anodic current at −0.3 $V_{Ag/AgCl}$ and an increase in the cathodic current as −0.7 $V_{Ag/AgCl}$, related to the oxidation of the $[MoS_4]^{2-}$ to MoS_3 species, and the

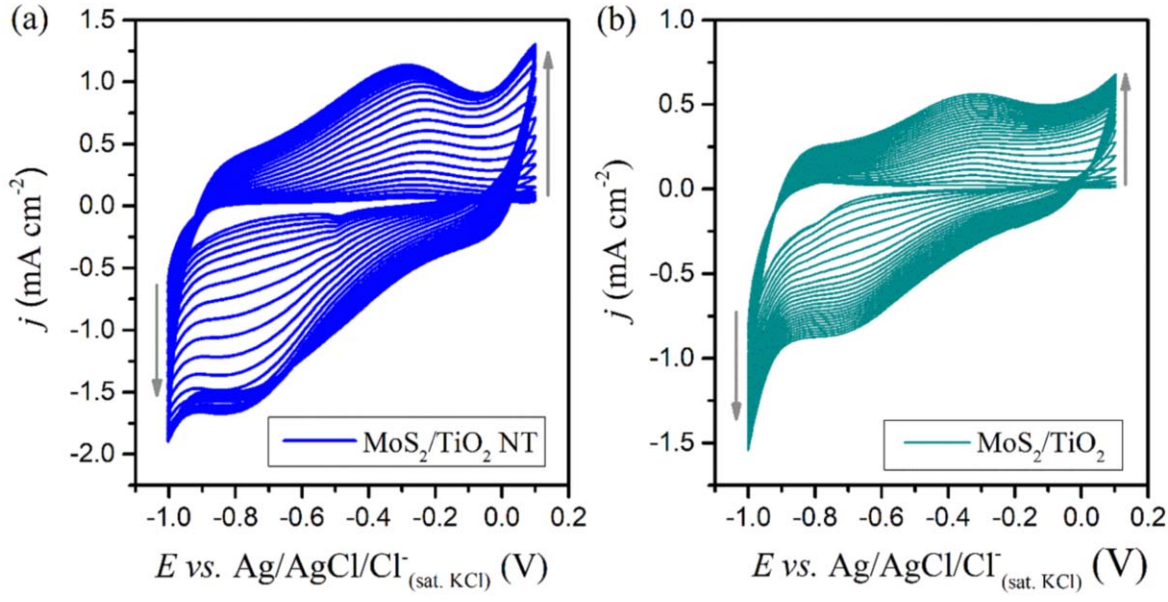

Figure 1. CVs for 25 cycles of MoS_x electrodeposition in (a) TiO_2 NT and (b) TiO_2 film substrates at 50 mV s^{-1} in 4 mmol l^{-1} $(NH_4)_2MoS_4$ and 0.1 mol l^{-1} $NaClO_4$ solution.

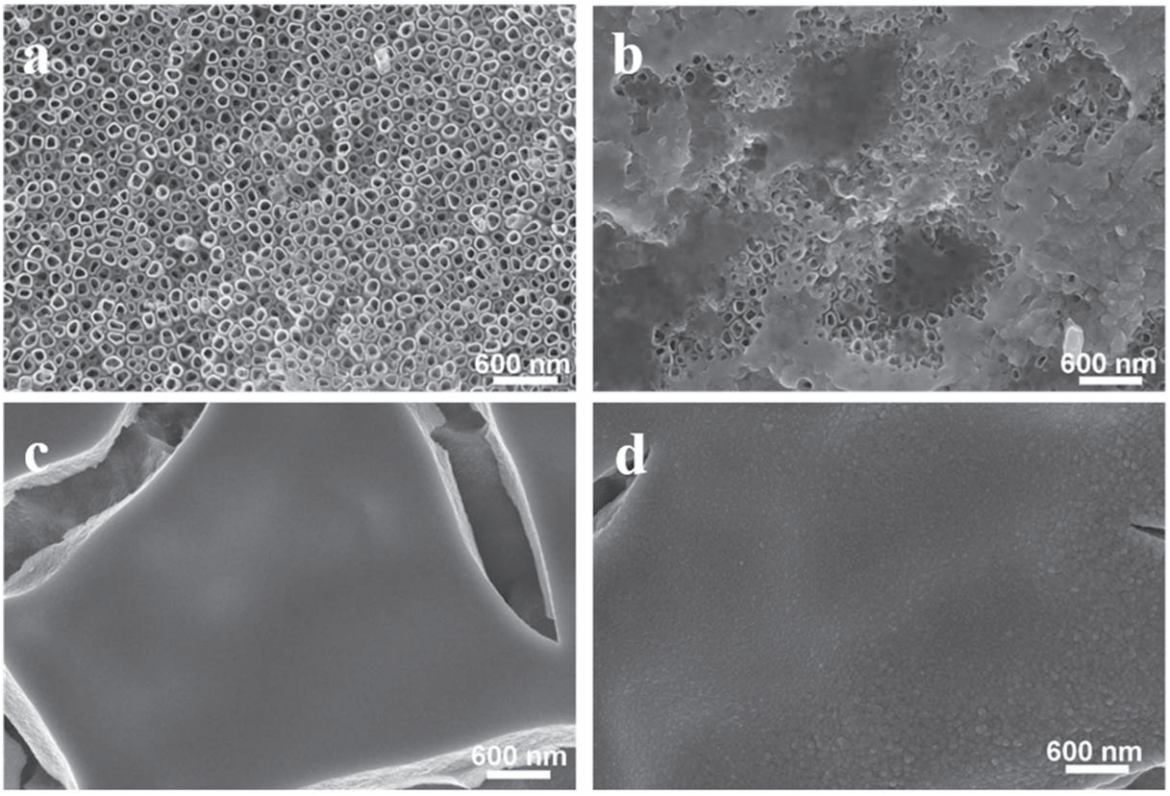

Figure 2. The SEM images of (a) un-modified TiO_2NT substrate, (b) the surface morphology of MoS_x catalyst film on the TiO_2NT substrate, (c) un-modified TiO_2 film substrate, and (d) the surface morphology of MoS_x catalyst film on the TiO_2 substrate.

reduction process to form MoS_2, respectively, as shown in Eqs. 4 and 5.[27]

$$[MoS_4]^{2-} \rightarrow MoS_3 + 1/8S_8 + 2e^- \quad [4]$$

$$[MoS_4]^{2-} + 2H_2O + 2e^- \rightarrow MoS_2 + 2HS^- + 2HO^- \quad [5]$$

The increasing anodic and cathodic currents indicate the MoS_x film growth on both substrates and the greater incorporation of the species involved in the film's deposition as the number of cycles increases from 1 to 25 (grew arrays, Figs. 1a, 1b). It is well known that the electrodeposition technique provides the molybdenum sulfide in the amorphous form,[27–31] and the XRD pattern of the as-obtained MoS_x film on the TiO_2 NT (Figure S1 in the Supporting Information; SI (available online at stacks.iop.org/JES/169/026519/mmedia)) and TiO_2 film (Fig. S2) confirms this by no diffraction peaks other than those in the same location and shape as the substrates. Beyond that, was confirmed too that both TiO_2 semiconductor substrates (nanotubes and film) were in the anatase form.

Scanning electron microscopy was used to characterize the morphology and verify the nucleation pattern of the MoS_x catalyst film on both substrates. Firstly, Fig. 2a presents the unmodified TiO_2NT in which is possible to see the nanotubes, while the TiO_2 film is presented in Fig. 2c with its typical morphology known as cracked clay.

Analyzing the growth pattern of MoS_x on TiO_2NT and TiO_2 film substrates, an interesting result was verified. The MoS_x growth on the TiO_2NT substrate occurs in a not homogeneous form (Fig. 2b) resulting in the formation of clusters above the entire substrate surface with the suppression of in-plane oriented growth. On the other hand, the deposition on the TiO_2 film (Fig. 2d) results in a homogeneous and in-plane MoS_x film. In comparison, even the two compositional substrates were formed by the TiO_2 semiconductor in

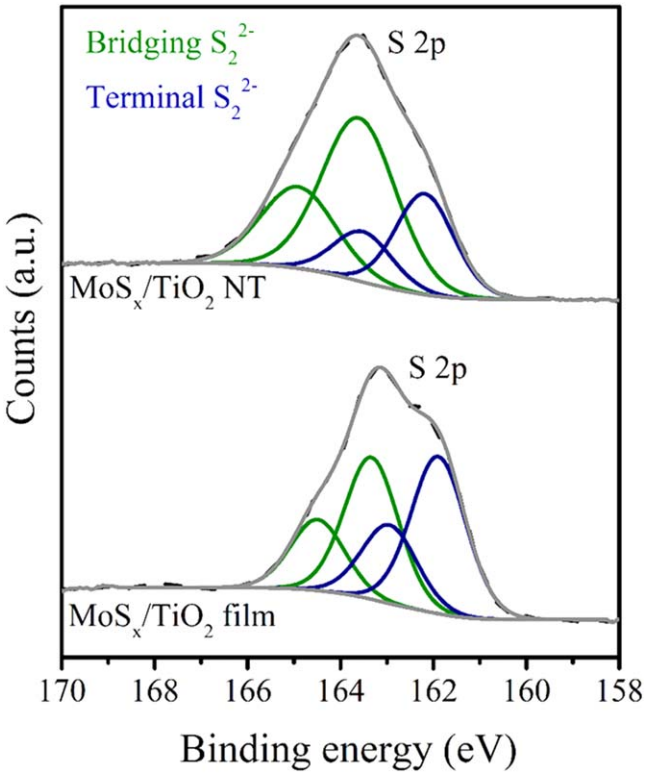

Figure 3. High-resolution XPS spectra of S 2p region of MoS_x film on TiO_2 NT and TiO_2 film substrates.

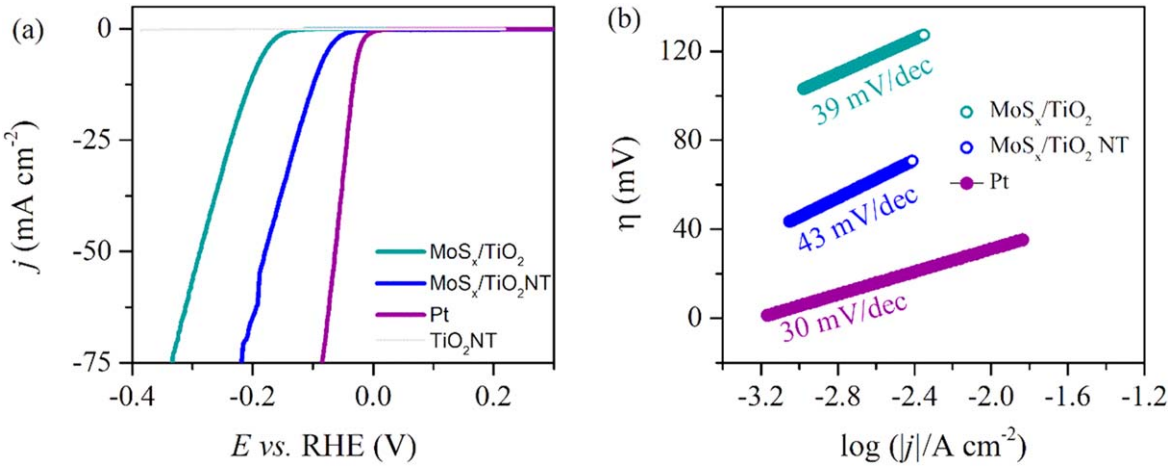

Figure 4. (a) Polarization curve in H_2SO_4 solution (pH 0.3) at 5 mV s^{-1}, (b) Tafel plot for MoS_x/TiO_2, MoS_x/TiO_2NT and Pt.

the anatase form, the nanotubes configuration promotes the suppression of the continuous growth of MoS_x, resulting in a stacked deposition. With a higher lamellar deposition, the MoS_x lateral size exposition, with the abundant and accessible active edge sites are more exposed to the H adsorption, is favoured on TiO_2NT. Due to this physical characteristic, is expected to obverse the enhanced activity for HER of the MoS_x/TiO_2NT electrode.

Among the possible S configurations, it is known that the S-bridging one is the most active for the H adsorption at the MoS_x edge sites. In this sense, X-ray photoelectron spectroscopy (XPS) was used to verify the surface chemical composition and valence state of the S and Mo atoms on the MoS_x deposit over TiO_2 NT and TiO_2 film.

Figure 3 shows the high-resolution XPS data in the S 2p region, composed of terminal S_2^{2-} and bridging S_2^{2-} configurations each one with two doubles. For the MoS_x on TiO_2 film the higher binding energies (BE) doublet, corresponding to S bridging configuration (S-brid), are located at 163.4 eV and 164.5 eV, while the lower BE doublet, related to S terminal configuration (S-term) is at 162.0 eV and 163.0 eV. For the MoS_x on TiO_2 NT the S 2p higher BE doublets are located at 163.7 eV and 165.0 eV, and the lower BE doublets at 162.2 eV and 163.6 eV. The atomic percentage calculations show 47% and 53% for S-brid and S-term, respectively, for the MoS_x in TiO_2 (Table S2). However, by the increasing exposure of the MoS_x lateral size with the S active sites in the MoS_x deposit on TiO_2NT substrate, the atomic percentage of the S-brid atomic was higher, reaching a value equal to 67% (Table S2). The Mo 3d spectra for the MoS_x on TiO_2NT (Fig. S3a) show one major doublet at 229.7 eV and 233.0 eV, and a minor one at 230.7 eV and 234.5 eV related to the Mo^{4+} and Mo^{5+} oxidation state, respectively. In this case, the atomic content presents a similar structural change observed for the S 2p spectra, with a decrease in the proportion of Mo^{5+} (Fig. S3, Table S3), indicating a lower molybdenum atoms content. For the MoS_x film in TiO_2 film (Fig. S3b), the same corresponding peaks for Mo^{4+} (229.7/230.7 eV) and Mo^{5+} (233.0/234.5 eV) species were observed. One more doublet related to Mo^{6+}, indicating the film oxidation during the storage before analyzes. The S/Mo ratio for the MoS_x/TiO_2 film was only 2.1, while for the MoS_x/TiO_2NT this ratio was 2.4 (Table S4). Thus, it was observed an increase of the entire S atoms due to the high exposure of the MoS_x lateral size with the non-oriented in-plane MoS_x deposit over the TiO_2 nanotubes.

The electrocatalytic activity for HER of the MoS_x/TiO_2NT and MoS_x/TiO_2 film electrodes were evaluated by linear sweep voltammetry at 5 mV s^{-1} in an H_2SO_4 acid solution (pH 0.3). Figure 4a presents the polarization curves and the non-catalytic response of the TiO_2NT substrate can be observed by the absence of density current values. However, with the MoS_x deposit onto the TiO_2NT and TiO_2 film substrates, an exponential increase of current density values appears as a consequence of the applied potential, indicating the HER catalytic activity of both tested electrodes (MoS_x/TiO_2NT and MoS_x/TiO_2). Besides that, it is possible to see that the catalytic behavior of the MoS_x/TiO_2NT seems very similar and closer to the Pt noble metal catalyst, indicating the high activity of this MoS_x-based electrode. The onset potential value, defined as the potential at the current density of −1 mA cm^{-2},[32] expresses this behavior in the sense that the value for the Pt catalyst is −6 mV, while for the MoS_x/TiO_2NT is −46 mV, reflecting an increase of only 40 mV. The polarization results were used to construct the Tafel plot and Fig. 4b presents the linear portion fitted by the Tafel equation (Eq. 1).

Table I. HER electrocatalytic activities of MoS_x deposited on TiO_2 and TiO_2NT substrates.

Electrode	$-\eta_{10}$ (mV)	b (mV dec^{-1})	j_0 (μA cm^{-2})
MoS_x/TiO_2	190 ± 4.20	39	0.15
MoS_x/TiO_2NT	93 ± 7.5	43	91.0

The effects of the increase S atom content performed by the MoS_x deposit on TiO_2NT are seen on the enhanced electrochemical parameters used to evaluate the HER catalysis (Table I). The overpotential needs to reach a density current of −10 mA cm^{-2} is reduced from 190 mV to 93 mV, and this value is the smaller one for MoS_x deposit on TiO_2NT-based supports presents in the literature (Table SI). The Tafel slope (b) is correlated to the mechanistic process for HER at the electrocatalytic interface and the values present in Table I reflect the Tafel mechanism occurring in both electrodes.[33] The exchange current density (j_0), a kinetic parameter that indicates the intrinsic catalytic activity of the electrode material at potential equilibrium (0 V_{RHE}), reflects the electron transfer rate in the catalyst/solution interface.[34] The increase S atom content for the MoS_x/TiO_2NT electrode results in the higher j_0 value equal to 91.0 μA cm^{-2}. When comparing with the $j_0$value for the MoS_x/TiO_2 (0.15 μA cm^{-2}) the increase was 600 times.

Cyclic voltammograms as a function of scan rate (Fig. S4) were performed to calculate the electrochemical surface area (Eq. S1, Fig. S5) and obtain the electrochemically active surface area (ECSA, Table SV) of the samples. As observed in Fig. 5a, the higher ECSA value was estimated for the MoS_x/TiO_2NT electrode. These results were used to normalize the activities to obtain the inherent catalytic properties of the MoS_x-based catalyst. The normalized polarization

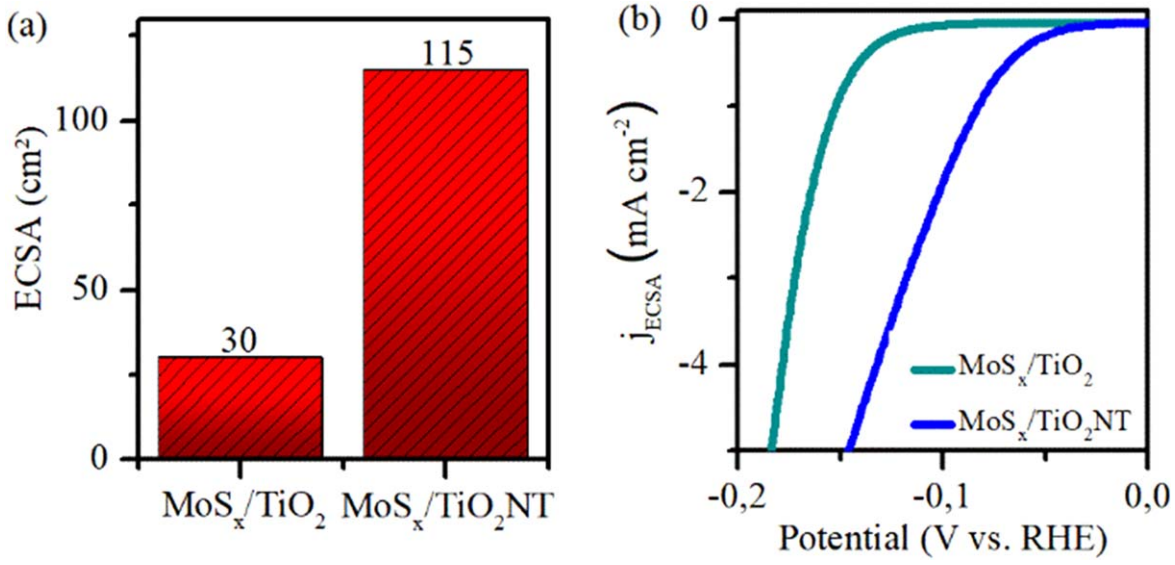

Figure 5. (a) ECSAs and (b) HER polarization curves at 5 mV s^{-1} normalized by ECSA values, for the MoS_x/TiO_2 and MoS_x/TiO_2NT electrodes.

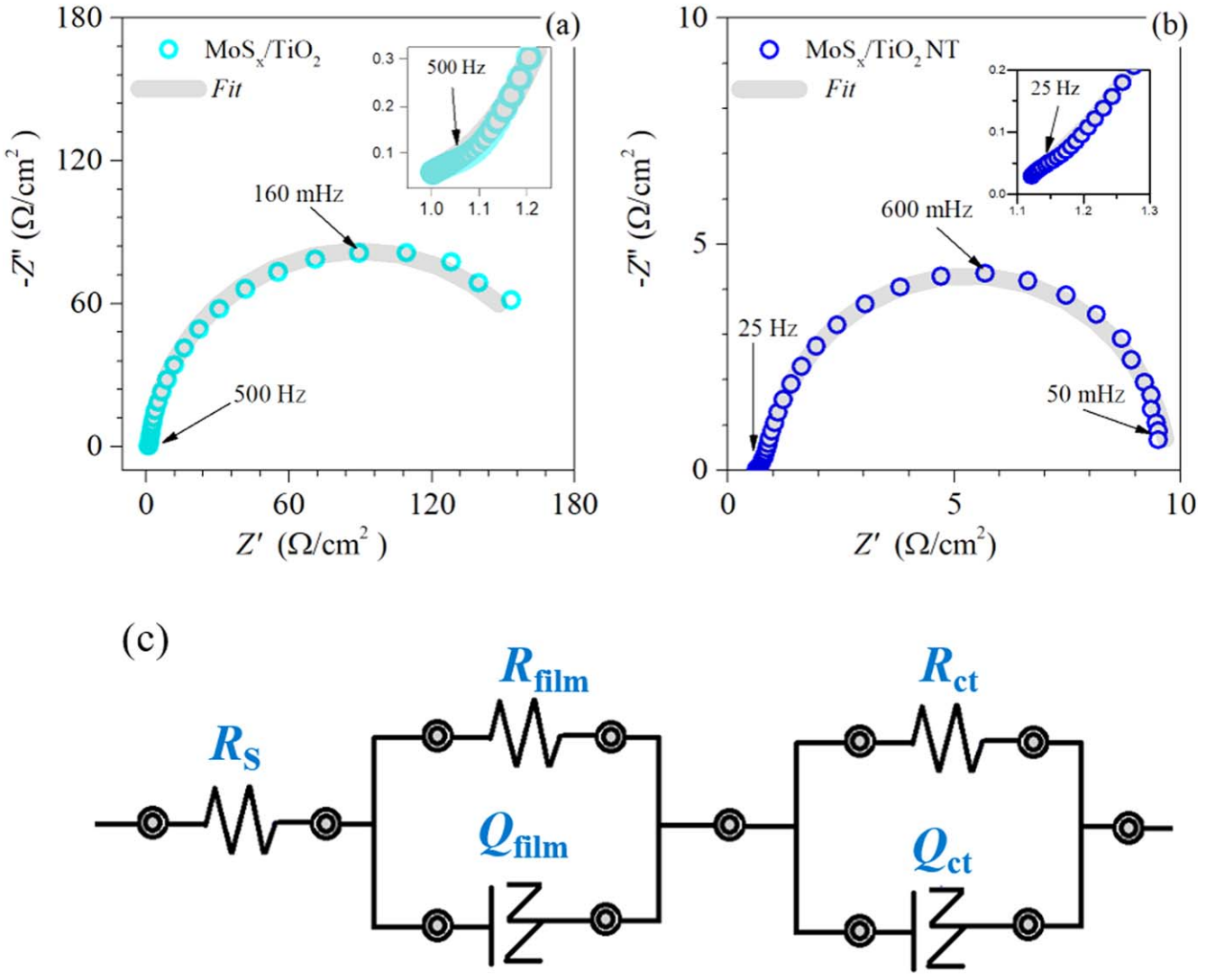

Figure 6. Nyquist plot for (a) MoS_x/TiO_2 and (b) MoS_x/TiO_2NT. (c) Equivalent circuit for EIS measurements.

curve is presented in Fig. 5b, reflecting the greater real surface area truly exposed to the electrolyte for H adsorption in the MoS_x/TiO_2NT electrode.

The turnover frequency (TOF) was investigated using the procedure proposed by Benck and co-workers[26] with the steps described on SI (Table S5). This factor is an important evaluation of the intrinsic property of the catalyst because presents the number of hydrogen molecules produced per catalytic site and per unit time.[35] The TOF value at −200 mV for MoS_x/TiO_2 was 1.45 s^{-1} while for the MoS_x/TiO_2NT an increased value 1.6 times higher was observed, reaching 2.28 s^{-1}.

EIS was performed to analyze the charge transport of MoS_x film on different TiO_2-based substrates. Figure 6 shows the Nyquist plot for MoS_x on TiO_2 (Fig. 6a) and TiO_2NT (Fig. 6b) substrates.

For both electrodes, two semicircles are seen: on the high-frequency range with small intensity (insert Fig. 6) and at lower frequency values with large intensity. The small semicircle is correlated to resistance and pseudo-capacitance between the MoS_x film/substrate contact (R_{film} and Q_{film}, respectively). The large semicircle refers to the resistance and pseudo-capacitance of the charge transfer process (R_{ct} and Q_{ct}, respectively).[36,37] To estimate the values of each circuit element, the equivalent electric circuit, shown in Fig. 6c, was used to fit all measures. Table S6 shows the values of R_s, R_{film}, and R_{ct} for all coatings. R_s and R_{film} were similar for all substrates, indicating that the feasibility of grown MoS_x films is the same between the different substrates. On the other hand, a very significant change in R_{ct} was observed, and this resistance is significantly reduced when TiO_2 is in the nanotube morphology. This data corroborates the greater content of S active sites and the higher value observed for the j_o that was observed for the MoS_x/TiO_2NT electrode.

Conclusions

The strategy of depositing MoS_x on TiO_2 nanotubes substrate resulted in the non-oriented growth of the film in the substrate plan. This characteristic growth allowed a greater exposure of the MoS_x film lateral size and, therefore, a higher proportion of the bridging S configuration was achieved, when compared with the MoS_x on TiO_2 film substrate. The atomic percent of bridging S to the entire S content of MoS_x was 67% with an S/Mo ratio equal to 2.4. The MoS_x/TiO_2NT presents excellent HER activity, reaching −10 mA cm^{-2} at 93 mV with a smaller Tafel slope of 43 mV dec^{-1} and a higher exchange current density of 91 μA cm^{-2}. The ECSA normalized density showed that the truly active sites for H adsorption were exposed on the catalyst/solution interface. This substrate morphology effect for achieving a greater lateral size exposure of MoS_x deposit, prepared by electrodeposition, is a facile one-step approach to prepare a highly active MoS_x-based catalyst for HER. This study enables further approaches to enhance the application for hydrogen production.

Acknowledgments

The authors thank the Laboratory of Structural Characterization (LCE/DEMa/UFSCar) for the general facilities and Professor Valmor Mastelato for the XPS measures. The authors are grateful to the following Brazilian research funding agencies for the financial support provided during this research: São Paulo Research Foundation (FAPESP, grant #2013/07296-2, #2014/50249-8, #2017/12794-2, #2017/11986-5, #2018/16401-8, #2018/02950-0), Coordenação de Aperfeiçoamento de Pessoal de Nível Superior-Brasil (CAPES)—Finance Code 001 and Conselho Nacional de Pesquisa e Desenvolvimento (CNPq). The authors also gratefully acknowledge the support of Shell and the strategic importance of the support given by ANP (Brazil's National Oil, Natural Gas, and Biofuels Agency) through the R&D levy regulation.

ORCID

Marina Medina https://orcid.org/0000-0003-0634-3613
Patricia G. Corradini https://orcid.org/0000-0003-1499-7967
Juliana F. de Brito https://orcid.org/0000-0002-6014-7739

References

1. A. Eftekhari, *Int. J. Hydrogen Energy*, **42**, 11053 (2017).
2. K. Ojha, S. Saha, P. Dagar, and A. K. Ganguli, *Phys. Chem. Chem. Phys.*, **20**, 6777 (2018).
3. J. Zhu, L. Hu, P. Zhao, L. Y. S. Lee, and K. Y. Wong, *Chem. Rev.*, **120**, 851 (2020).
4. Y. Wang, Z. Zhang, Y. Mao, and X. Wang, *Energy Environ. Sci.*, **13**, 3993 (2020).
5. N. Cheng et al., *Nat. Commun.*, **7**, 1 (2016).
6. Z. Pu et al., *Nano-Micro Lett.*, **12**, 21 (2020).
7. T. F. Jaramillo, K. P. Jørgensen, J. Bonde, J. H. Nielsen, S. Horch, and I. Chorkendorff, *Science*, **317**, 100 (2007).
8. G. Li et al., *J. Am. Chem. Soc.*, **138**, 16632 (2016).
9. C. G. Morales-Guio and X. Hu, *Acc. Chem. Res.*, **47**, 2671 (2014).
10. Y. Deng, L. R. L. Ting, P. H. L. Neo, Y. Zhang, A. A. Peterson, and B. S. Yeo, *ACS Catal.*, **6**, 7790 (2016).
11. C. H. Lee, S. Lee, G. S. Kang, Y. K. Lee, G. G. Park, D. C. Lee, and H. I. Joh, *Appl. Catal. B Environ.*, **258**, 117995 (2019).
12. C. H. Lee, S. Lee, Y. K. Lee, Y. C. Jung, Y. I. Ko, D. C. Lee, and H. I. Joh, *ACS Catal.*, **8**, 5221 (2018).
13. L. R. L. Ting, Y. Deng, L. Ma, Y. J. Zhang, A. A. Peterson, and B. S. Yeo, *ACS Catal.*, **6**, 861 (2016).
14. J. Kibsgaard, T. F. Jaramillo, and F. Besenbacher, *Nat. Chem.*, **6**, 248 (2014).
15. C. Tsai, F. Abild-Pedersen, and J. K. Nørskov, *Nano Lett.*, **14**, 1381 (2014).
16. X. Qiu, Y. Huang, Z. Nie, B. Ma, Y. Tan, Z. Wu, N. Zhang, and X. Xie, *Nanoscale*, **12**, 1109 (2020).
17. Z. Liu, X. Zhang, B. Wang, M. Xia, S. Gao, X. Liu, A. Zavabeti, J. Z. Ou, K. K. Zadeh, and Y. Wang, *J. Phys. Chem. C*, **122**, 12589 (2018).
18. F. Du, H. Lu, S. Lu, J. Wang, and Y. Xiao, *Int. J. Hydrogen Energy*, **43**, 3223 (2018).
19. C. Meng, Z. Liu, T. Zhang, and J. Zhai, *Green Chem.*, **17**, 2764 (2015).
20. X. Song, G. Chen, L. Guan, H. Zhang, and J. Tao, *Appl. Phys. Express*, **9**, 0 (2016).
21. J. F. de Brito, J. A. L. Perini, S. Perathoner, and M. V. B. Zanoni, *Electrochim. Acta*, **306**, 277 (2019).
22. G. G. Bessegato, J. C. Cardoso, B. F. Da Silva, and M. V. B. Zanoni, *J. Photochem. Photobiol. A Chem.*, **276**, 96 (2014).
23. L. K. Tsui, N. T. Nguyen, L. Wang, R. Kirchgeorg, G. Zangari, and P. Schmuki, *Electrochim. Acta*, **155**, 244 (2015).
24. M. Medina and P. G. Corradini, *J. Braz. Chem. Soc.*, **30**, 2210 (2019).
25. D. Li, C. Batchelor-McAuley, and R. G. Compton, *Appl. Mater. Today*, **18**, 1 (2020).
26. J. D. Benck, Z. Chen, L. Y. Kuritzky, A. J. Forman, and T. F. Jaramillo, *ACS Catal.*, **2**, 1916 (2012).
27. H. Vrubel and X. Hu, *ACS Catal.*, **3**, 2002 (2013).
28. P. Yang, B. Wang, and Z. Liu, *Int. J. Hydrogen Energy*, **43**, 23109 (2018).
29. M. Shang, H. Qi, C. Du, H. Huang, S. Wu, J. Zhang, and W. Song, *Sensors Actuators B: Chem.*, **266**, 71 (2018).
30. D. Merki, S. Fierro, H. Vrubel, and X. Hu, *Chem. Sci.*, **2**, 1262 (2011).
31. D. Merki, H. Vrubel, L. Rovelli, S. Fierro, and X. Hu, *Chem. Sci.*, **3**, 2515 (2012).
32. S. X. Zou and Y. Zhang, *Chem. Soc. Rev.*, **44**, 5148 (2015).
33. S. Anantharaj, S. R. Ede, K. Karthick, S. S. Sankar, K. Sangeetha, P. E. Karthik, and S. Kundu, *Energy Environ. Sci.*, **11**, 744 (2018).
34. A. P. Murthy, J. Theerthagiri, and J. Madhavan, *J. Phys. Chem. C*, **122**, 23943 (2018).
35. R. Bose, M. Seo, C. Y. Jung, and S. C. Yi, *Electrochim. Acta*, **271**, 211 (2018).
36. H. Vrubel, T. Moehl, M. Grätzel, and X. Hu, *Chem. Commun.*, **49**, 8985 (2013).
37. K. K. Upadhyay, T. Nguyen, T. M. Silva, M. J. Carmezim, and M. F. Montemor, *Mater. Chem. Phys.*, **216**, 413 (2018).